HIGH-RESOLUTION RADAR ANALYSIS DURING TORNADOGENESIS FROM OU-PRIME ON 10 MAY 2010

D. Bodine[1,2,*], R. D. Palmer[1,2], C. Ziegler[3], and P. L. Heinselman [3]

[1] School of Meteorology, The University of Oklahoma, Norman, OK, U.S.A.
[2] Atmospheric Radar Research Center, The University of Oklahoma, Norman, OK, U.S.A
[3] NOAA/OAR National Severe Storms Laboratory, Norman, OK, U.S.A

1. INTRODUCTION

The 10 May 2010 tornado outbreak devastated parts of central Oklahoma, causing two fatalities, dozens of injuries, and major property damage. The first author's house was struck by the southern EF1 Norman tornado (Fig. 1: top left and right), although the resulting damage was minor compared to EF3 and EF4 damage elsewhere. The outbreak produced 35 tornadoes, including seven strong and two violent tornadoes (Fig. 1: bottom).

The proximity of the tornado outbreak to Oklahoma City presented a relatively uncommon opportunity to obtain close observations of supercells and significant tornadoes from fixed-site radars. At least 11 tornadoes occurred within 50 km of the University of Oklahoma's (OU's) new high-resolution Polarimetric Radar for Innovations in Meteorology and Engineering (OU-PRIME; Palmer et al., 2009, 2010), located at the National Weather Center (NWC). In one case, an EF4 tornado initiated just 200 yards south of NWC! A companion paper (Bodine et al., 2010) discusses the evolution of the Norman, Oklahoma EF4 tornado's parent supercell (Supercell B) and its interactions with the supercell that produced the EF4 tornado originating in Moore, Oklahoma (Supercell A) and other convection forming along the rear-flank downdraft (RFD) gust front.

This paper focuses on the evolution of sub-storm-scale vortices in the Moore, Oklahoma supercell, and the evolution of the storm during tornadogenesis and tornado intensification. During tornadogenesis, strong vortices were observed within the RFD region, including within reflectivity flares extending from the hook echo, and along the RFD gust front. Several characteristics of the vortices are analyzed to understand:

- the origins of the vortices
- the four-dimensional evolution of the vortices
- what interactions occur between vortices of different scales
- the role of these small-scale vortices in tornadogenesis

* *Corresponding author address:* David Bodine, University of Oklahoma, School of Meteorology, 120 David L. Boren Blvd., Rm 4630, Norman, OK 73072-7307; e-mail: bodine@ou.edu

The second part of the paper discusses the evolution of the Moore supercell during tornadogenesis and tornado intensification.

Section 2 provides a background on supercell thunderstorms and sub-storm-scale vortices. The quantitative methods used to investigate the sub-storm-scale vortices and a description of OU-PRIME are presented in Section 3. An analysis of OU-PRIME data from the 10 May 2010 case is presented in Section 4, including an investigation of reflectivity flares, RFD gust front vortices, mesocyclone and mesoanticyclone evolution, tornadogenesis, and tornado evolution. The paper concludes with a discussion of the results in Section 5, followed by the conclusions of the paper in Section 6.

2. BACKGROUND

The defining feature of supercell thunderstorms is a persistent, rotating updraft, or mesocyclone (Browning, 1964). The tilting of environmental, low-level vorticity, which is subsequently stretched by intense vertical velocities in the updraft, produces vorticity on the order of 0.01 s^{-1} within the mesocyclone (e.g., Burgess et al., 1982). Although most significant tornadoes occur with supercells, the presence of a mesocyclone alone is insufficient for tornadogenesis. Recently, Trapp et al. (2005) found that only 15 and 40 percent of mid- and low-level mesocyclones produced tornadoes, respectively. The capability to more accurately discern between tornadic and nontornadic supercells remains a desirable goal, requiring a more complete understanding of the relationship between the mesocyclone and the tornado as well as an understanding of what characteristics of the parent storm may facilitate tornadogenesis in some cases, but not others.

The rear-flank downdraft (RFD) in supercell thunderstorms appears to be critical for tornadogenesis, although the understanding of the dynamic processes relating the RFD and tornadogenesis are not fully understood (Markowski, 2002). Precipitation falling in the RFD is often observed in radar reflectivity as a hook echo, or a curved appendage extending from the right-rear flank of the supercell. Two primary hypotheses have emerged to explain the origins of the hook echo. In the first hypothesis, the hook echo forms due to the advection of precipitation around the

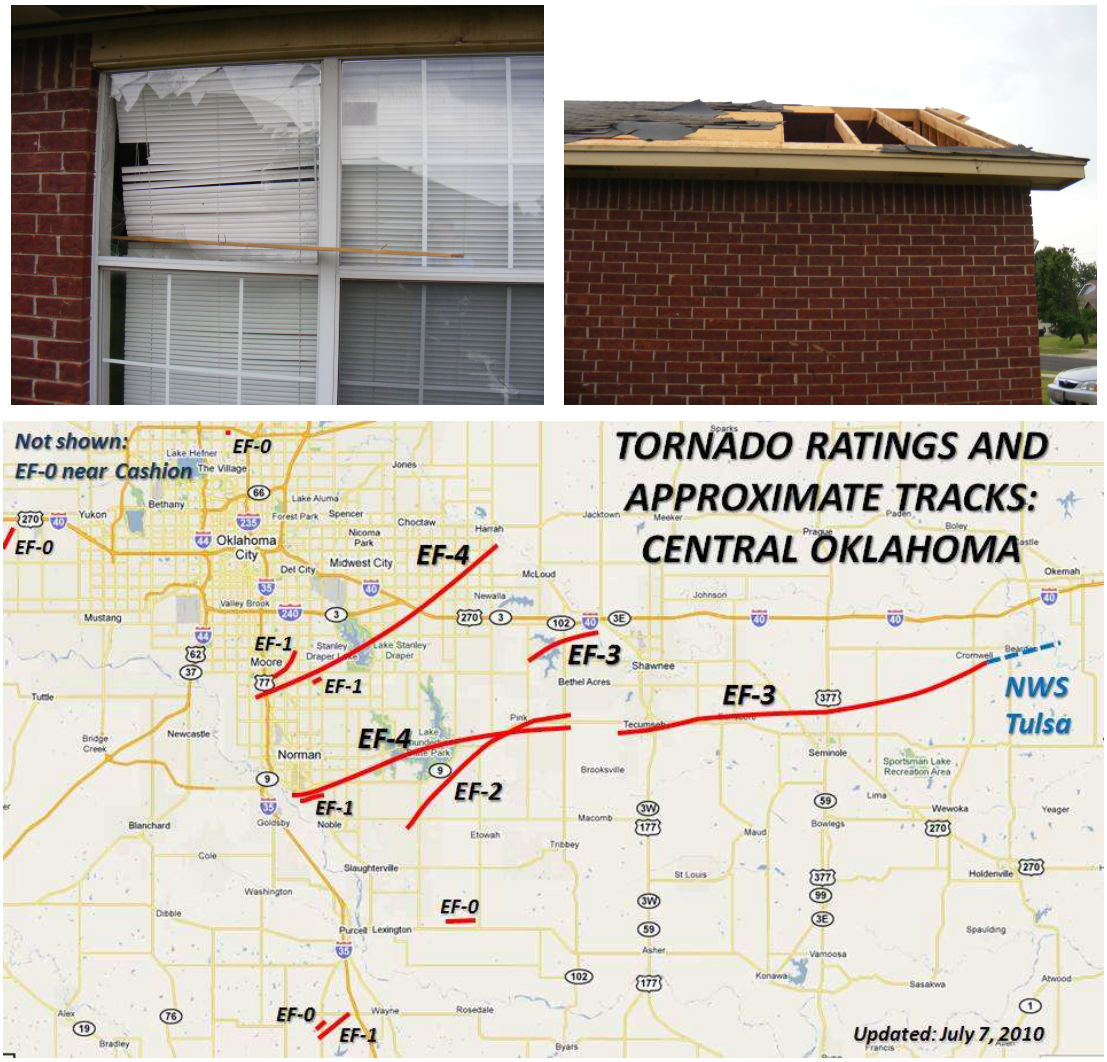

Figure 1: Tornado damage to the first author's house from the southern EF1 tornado in Norman, Oklahoma (top left and right). The damage paths from the 10 May 2010 tornadoes in central Oklahoma are shown in the bottom image. (courtesy of the Norman, Oklahoma National Weather Service Weather Forecast Office; NWS WFO)

mesocyclone (e.g., Fujita, 1958; Browning, 1964). In the second hypothesis, hook echoes form from the descent of precipitation within the RFD (e.g., Forbes, 1981). Markowski (2002) suggests that both processes could contribute to hook echo formation, and the contributions of each process may vary among supercells and even during a single supercell's lifetime. Recently, Magsig et al. (2002) found that horizontal advection did not fully explain the evolution of a hook echo in a tornadic supercell.

Although much of the literature focuses on the role of the mesocyclone or RFD in tornadogenesis, modeling and observational studies have revealed other vortices within supercells exhibiting vorticity on the same order of magnitude as the mesocyclone. In some cases, these vortices may instigate tornadogenesis. Simulations by Wicker and Wilhelmson (1995) revealed several 1-km-scale vortices, with vorticity magnitudes exceeding 0.1 s^{-1}. Vorticity magnitudes of mesocyclone strength have been observed in small-scale vortices detected by mobile radars. Bluestein et al. (1997) observed counterrotating, 500-m-scale vortices in a supercell thunderstorm along the RFD gust front. Given that a symmetric vortex pair was produced, they speculated that the vorticity was generated by tilting environmental horizontal vorticity. Bluestein et al. (2003) observed vortices along the RFD gust front with diameters of 100 – 200 m, which coexisted with vortices at a scale of 500 m. During tornadogenesis, a larger scale vortex (500-m scale) merged with one of the smaller scale vortices (100 – 200 m scale). They suggested that interactions between vortices of different scales may be necessary for tornadogenesis.

3. DATA AND METHODOLOGY

3.1. Data and post-processing

OU-PRIME collected rare polarimetric data during the 10 May 2010 tornado outbreak in central Oklahoma, capturing several supercells, and nearly a dozen tornadoes in close proximity to OU-PRIME. This paper examines OU-PRIME data from a supercell that produced an EF4 tornado in Moore, Oklahoma and parts of southern Oklahoma City, causing major property damage. The OU-PRIME data examined in this study were collected between 2200 – 2240 UTC.

A detailed technical description of OU-PRIME is presented in Palmer et al. (2010), although it is described here briefly. OU-PRIME possesses a 0.45° beamwidth, and range resolution up to 25 m with oversampling, making it one of the highest resolution C-band polarimetric radars in the world. During the 10 May 2010 outbreak, the radar employed a longer pulse width to increase sensitivity, so the range resolution was 125 m. In addition to high spatial resolution, OU-PRIME has a peak transmit power of 1 MW, providing excellent sensitivity. During the 10 May 2010 outbreak, sector mode scanning by OU-PRIME improved update times to 2–3 min without compromising data quality (e.g., without decreasing the number of pulses). The radar operated with an unambiguous velocity of 16 m s^{-1}, hence significant velocity folding occurred within high shear regions such as within the tornado. To improve the unambiguous velocity, future plans include implementing methods for increasing the maximum unambiguous velocity, such as a staggered PRT (Sirmans et al., 1976).

After data collection, several steps were taken to generate high quality radar data. First, clutter filtering was applied to the time series data, and then moment data were produced using the multi-lag estimator (Zhang et al., 2004; Lei et al., 2009). After moment data were obtained, the National Center for Atmospheric Research (NCAR) Solo-II software package was employed to remove noise and second-trip echoes, and to dealias OU-PRIME velocity data (Oye et al., 1995). A signal-to-noise threshold of -5 dB was applied to all fields to remove suspect data in noisy regions. To further reduce noise and outliers, a 3-by-3 median filter was applied to all of the gates in the dealiased radial velocity field. The quantitative analyses described below use the resulting filtered velocity field.

3.2. Methodology

1) Single-Doppler dynamics

Single-Doppler vorticity and divergence (hereafter, vorticity and divergence) are computed from the filtered radial velocity data over the entire radar domain. For a range gate at gate g and azimuth a, vorticity, ζ, is computed by taking the velocity difference between two range gates spaced n_r radials from the range gate at (g, a),

$$\zeta(g,a) = 2\frac{v(g,a+n_r) - v(g,a-n_r)}{(2n_r+1)\Delta\theta}, \qquad (1)$$

where $\Delta\theta$ is the beamwidth in m. The divergence, δ, was computed similarly by taking the velocity difference between two range gates spaced n_g gates from the range gate at (g, a),

$$\delta(g,a) = \frac{v(g+n_g,a) - v(g-n_g,a)}{(2n_g+1)\Delta r}, \qquad (2)$$

where Δr is the gate width. For this study, values of 1 were chosen for both n_g and n_a.

Several important limitations exist for single-Doppler analyses of vorticity and divergence, so assumptions are made about the wind field being investigated. These quantities are often called "half divergence" or "half vorticity"

since only half of the horiziontal divergence or vertical vorticity are observed in a symmetric wind field (Smith and Elmore, 2004). In previous single-Doppler studies of vortices, vortices are generally assumed to be axisymmetric (e.g., Wurman et al., 2007). Hence, in this paper, vortices are assumed to be axisymmetric so the vorticity field is multiplied by a factor of two. The axisymmetric assumption for divergence is a poor assumption for most of the wind field within a supercell. Thus, divergence is only quantified for phenomena where asymmetric divergence is expected and where the unobserved (azimuthal) component of divergence is small. For example, divergence is computed along a radial perpendicular to the RFD gust front where the component of divergence parallel to the RFD gust front is likely much smaller.

After computing vorticity and divergence, the stretching term of the vorticity equation and vertical velocity are computed from these single-Doppler quantities. The vertical vorticity equation for an inviscid flow is,

$$\frac{\partial \zeta}{\partial t} = -\left(u\frac{\partial \zeta}{\partial x} + v\frac{\partial \zeta}{\partial y} + w\frac{\partial \zeta}{\partial z}\right) + \left(\frac{\partial u}{\partial z}\frac{\partial w}{\partial y} - \frac{\partial v}{\partial z}\frac{\partial w}{\partial x}\right) - \delta\zeta + \left[\frac{\partial}{\partial y}\frac{1}{\rho}\frac{\partial p}{\partial x} - \frac{\partial}{\partial x}\frac{1}{\rho}\frac{\partial p}{\partial y}\right], \quad (3)$$

where ζ is the vertical component of vorticity, u, v, and w are the Cartesian components of the wind field, δ is the horizontal divergence, ρ is density, and p is pressure. The terms on the right-hand side of Equation 3 are the horizontal and vertical advection of vorticity, tilting of horizontal vorticity into the vertical, stretching of vertical vorticity, and the solenoidal generation of vertical vorticity.

The stretching term of the vorticity equation and vertical velocity are computed along the RFD gust front where asymmetric divergence exists and the primary component of divergence is aligned along the radial. The stretching term, ζ_s, of the vorticity equation can be expressed in terms of radar observations using,

$$\frac{\partial \zeta_s}{\partial t}(g,a) = -\zeta(g,a)\delta(g,a), \quad (4)$$

where $\zeta(g,a)$ and $\delta(g,a)$ are computed as described by Equations 1 and 2. Vertical velocity, w, is estimated along the RFD gust front at gate (g,a,z) by integrating the continuity equation,

$$w(g,a,z(i)) = \sum_{i=1}^{N} -\delta(g,a,z(i))\Delta z, \quad (5)$$

where Δz is the distance between elevation angles and $z(i)$ is height in m AGL at the elevation angle, i. The divergence was assumed to vary linearly between the lowest observation of divergence and the surface where divergence is zero owing to friction (i.e., no-slip boundary conditions applied).

2) Vortex characteristics

Several methods were used to determine the spatiotemporal evolution of vortex position, intensity, and diameter. The position of the vortex was determined based on the maximum or minimum vorticity, and based on the maximum or minimum vorticity in a 3-by-3 region. For coherent vortices between volume scans, the position of the vortex at each elevation was corrected for translation based on the average velocity between volume scans. For transient vortices lasting less than one volume scan (e.g., RFD gust front vortices), advection correction was performed based on the mean motion of the gust front, providing a gust front relative position of the vortex. The vortex intensity is defined as the magnitude of the vorticity. Vortex intensity was computed based on the maximum magnitude of vorticity observed within the vortex, and based on the maximum magnitude of vorticity in a 3-by-3 region within the vortex. The latter method reduces the impact of suspect velocity data due to noise or uncertainty in unfolding the velocity data. Several different methods were employed to determine the vortex diameter. For isolated vortices such as the mesocyclone, the distance between the peak inbound and outbound velocities is used (e.g., French et al., 2008).

4. ANALYSIS AND DISCUSSION

4.1. Reflectivity flares and hook echo structure

During tornadogenesis, the hook echo exhibited a contorted structure with numerous reflectivity flares observed along the hook echo. In this section, the evolution of these flares and associated vortices are discussed and polarimetric radar data are examined to illuminate the origins of these flares. Reflectivity flares have been noted on the tip of the hook echo (e.g., Ziegler et al., 2001). Here, reflectivity flares moving along the periphery of the hook echo are investigated.

The first prominent reflectivity flares develop during the 2206 UTC volume scan. Along the hook echo, two counterrotating vortices are observed between 2206:31 and 2207:32 UTC about 2 km NE of the tip of the hook echo. At 2207:32 UTC at the 3.0° tilt (about 1.5 km AGL), the western reflectivity flare (Figure 2a) has anticyclonic azimuthal shear (Figure 2b) on the tip of the higher reflectivity region, with a computed vorticity of -4 X 10^{-2} s^{-1}. The eastern reflectivity flare possessed a cyclonic azimuthal shear region, with a slightly higher computed vorticity of 6 X 10^{-2} s^{-1}. At the 6.5° tilt, the reflectivity flare loses curvature even though anticyclonic azimuthal shear is still observed, and has a more uniform region of precipitation.

At the southern tip of the hook echo, an isolated anticyclonic azimuthal shear region is observed at the lowest tilt.

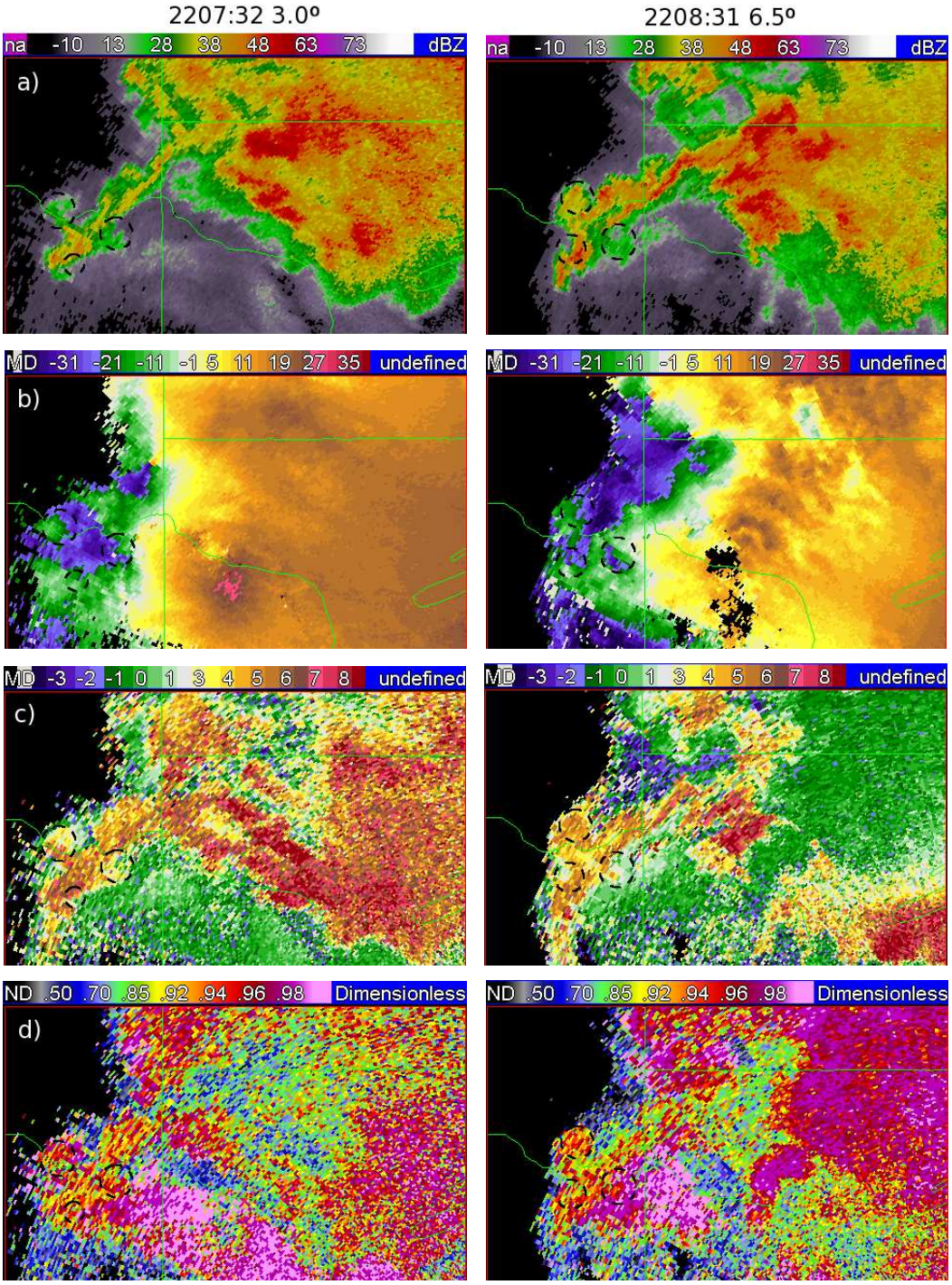

Figure 2: Reflectivity flares observed in a) reflectivity, b) radial velocity, c) differential reflectivity Z_{DR}, and d) cross-correlation coefficient ρ_{hv} at the 3.0° and 6.5° tilts during the 2206 UTC volume scan.

The anticyclonic azimuthal shear region exhibited vertical continuity, and appeared to translate northeast along the outer perphiery of the hook echo. At 3.0°, a reflectivity flare is observed associated with the anticyclonic azimuthal shear region, and exhibits polarimetric characteristics similar to precipitation in the hook echo, including high Z_{DR} and moderate ρ_{hv} values (Figure 2c,d). The anticyclonic flow alters the shape of the hook echo by horizontal advection of hydrometeors, as suggested by the weaker radial velocities in the flare and the polarimetric characteristics of the hydrometeors in the reflectivity flare, which are similar to the hook echo.

By the 2209 UTC volume scan, the two anticyclonic reflectivity flares have moved northeast along the outer portion of the hook echo. A similar vertical structure is observed in each reflectivity flare. In the lowest 1.5 km, the reflectivity values are relatively small (Z<30 dBZ), but the flare exhibits anticyclonic curvature. Above 1.5 km, the reflectivity values are higher, but the curvature is absent. At the 3.0° tilt (1.5 km AGL), the southern end of the hook echo exhibits a bowed appearance, which may be related to the RFD surge southeastward where strong negative radial velocities (<-30 m s^{-1}) are observed. At the 9.0° tilt, the southernmost reflectivity flare develops cyclonic curvature in reflectivity and is collocated with strong cyclonic shear. Just to the east of this cyclonic shear region, a counterrotating vortex pair is observed. The reflectivity field associated with the anticyclonic shear region exhibits anticyclonic curvature, whereas the cyclonic shear region is largely absent of precipitation. Intriguingly, the cyclonic shear is much stronger and more persistent, so horizontal advection does not fully explain the reflectivity structure observed.

During the initial RFD surge aloft at 2213:10 UTC, the leading edge of the hook echo develops a spearhead or hammerhead echo (Fujita and Byers, 1977; Magsig et al., 2002; Magsig and Dowell, 2004). The strongest winds at 4.0° are observed in a relatively small region (about 1 km wide), indicative of an RFD surge. At the same tilt, a spearhead echo is observed, characterized by a counterrotating pair of vortices. At the 6.5° tilt, the cyclonic member of the vortex pair becomes dominant and more precipitation is advected by the cyclonic member, consistent with observations by Wakimoto et al. (2006). As discussed previously, horizontal advection of hydrometeors is suggested by similar Z_{DR} and ρ_{hv} values in the spearhead echo compared to the hook echo. However, a small region of high ρ_{hv} and low to moderate Z_{DR} values are observed along the leading edge of the anticyclonic vortex in the spearhead echo.

The strong RFD winds advect the hydrometeors associated with the anticyclonic member of the spearhead echo downstream, producing a reflectivity flare. The reflectivity flare is observed on the southern side of the hook echo, along the leading edge of the maximum winds associated with the RFD surge. This reflectivity flare is observed at all tilts during the 2214 UTC volume scan, and appears to rotate around the southern tip of the hook echo (assuming vertical continuity). By 2217 UTC, radial velocities as high as -38 and -40 m s^{-1} are observed by OU-PRIME and KTLX at 0.2° and 0.5° (about 100 and 200 m AGL), respectively, indicating very strong, possibly damaging RFD winds near the surface. These strong RFD winds are still observed behind the reflectivity flare, which is now along the southern tip of the hook echo. The reflectivity flare is observed moving around the southern tip of the hook echo at 1.0° through 5.0° between 2217:46 and 2219:05 UTC.

The reflectivity flare observed moving north in the previous volume scan has moved north along the inside of the hook echo. During the 2220 UTC volume scan, two additional reflectivity flares are apparent on the outside of the hook echo, moving south between subsequent scans between 1.0° and 5.0°. The reflectivity flares exhibit very high ρ_{hv} (>0.98), low Z_{DR} (<1 dB), and low Z indicating small drop sizes and low drop concentration. Hence, the origin of the hydrometeors in the reflectivity flare is not likely from horizontal advection from the hook echo.

4.2. Mesoanticyclone structure and evolution

A persistent mesoanticyclone (e.g., Charba and Sasaki, 1971; Wilhelmson and Klemp, 1981) was observed in the northern part of the hook echo, where the hook echo connects to the right-rear flank of the supercell (Fig. 5). At 2220 UTC, the lowest tilt (about 100 m AGL) reveals an intense region of anticyclonic azimuthal shear, indicative of a mesoanticyclone, or perhaps even a weak, anticyclonic tornado. The strong anticyclonic azimuthal shear region is collocated with a kink in the hook echo. At the 3.0° tilt, a weak echo region is observed at the center of the mesoanticyclone. At the center of the mesoanticyclone, a small tornado vortex signature (TVS) is observed. The diameter of the mesoanticyclone at 0.2 and 3.0°is between 800-1000 m. At 6.5°, the diameter of the mesoanticyclone expands to about 1600 m, and a full ring of heavier precipitation surrounds the mesoanticyclone, indicating horizontal advection of precipitation around the mesoanticyclone. The flow within the mesoanticyclone becomes asymmetric, evident by an embedded TVS located just southwest of the center of the mesoanticyclone.

The evolution of the vorticity of the mesoanticyclone between 2212 and 2220 UTC is plotted in Figure 6. At the lowest tilt (0.2° or about 100 m AGL), the magnitude of low-level vorticity increases as a function of time, reaching a maximum value of -7 X 10^{-2} s^{-1} at 2220 UTC. Further aloft, the magnitude of vorticity generally increases as a function of height. However, by 2220 UTC, the magntiude

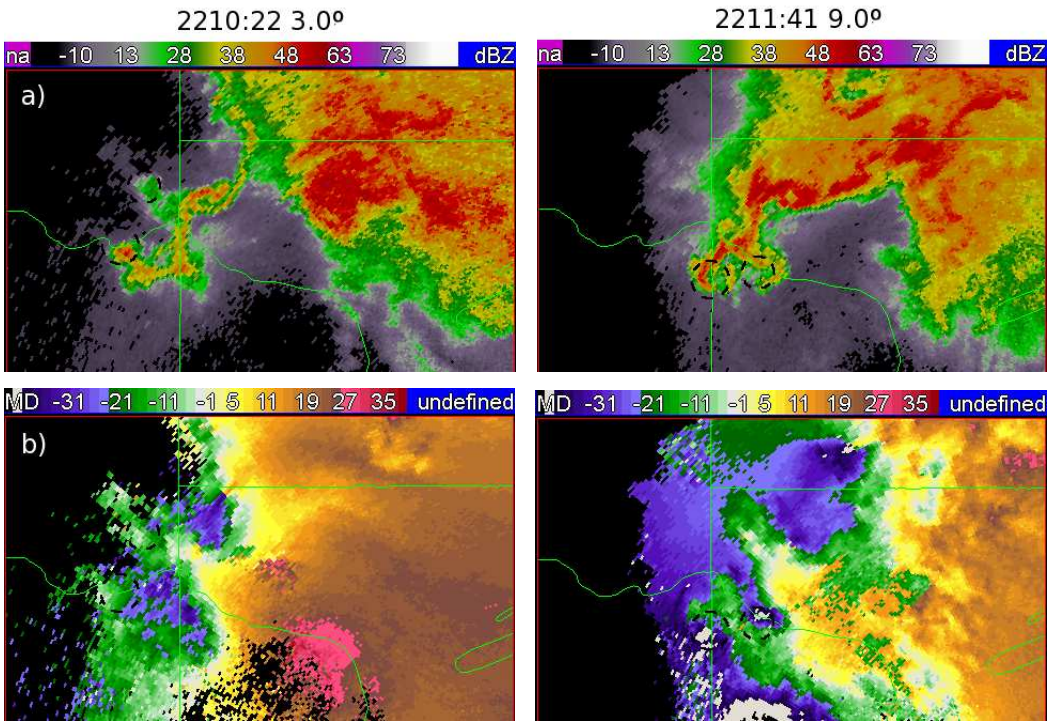

Figure 3: Reflectivity flares observed in a) reflectivity, and b) radial velocity at the 3.0° and 9.0° tilts during the 2209 UTC volume scan.

of vorticity actually decreases above 2 km. After correcting for advection, the mean vortex position (Figure 7) revealed that the mesoanticyclone is more tilted in the horizontal than the vertical, with a mean tilting angle of 29.5°. Remarkably, even with this orientation, the mesoanticyclone still produces strong vertical vorticity of mesocyclone strength and perhaps even produces a weak tornado.

4.3. RFD Gust Front vortices

1) Vortex characteristics

Along the RFD gust front, azimuthal shear regions indicative of vortices along the gust front were observed prior to tornadogenesis. Prominent RFD gust front vortices develop during the 2220 UTC volume scan, and select tilts are shown in Figure 8. The mean vortex diameter was computed for the vortices demarcated by the black circles. At the 0.2° and 1.0° tilts, the mean diameter of the RFD vortices was about 500 m. At the 3.0° and 4.0° tilts, the mean diameter increased to 770 m and 880 m, respectively, indicating that the vortex diameter increased in height over the lowest 800 m. In addition to increasing vortex diameter with increasing height, the RFD vortices decrease in concentration. In Figure 8, the vortices at lower tilts (about 100 – 200 m AGL)

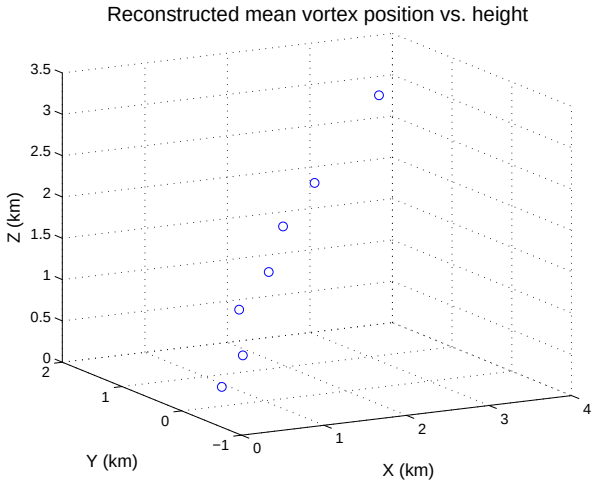

Figure 7: Mean vortex position as a function of height, corrected for storm motion. The mean tilting angle of the mesoanticyclone is 29.5°.

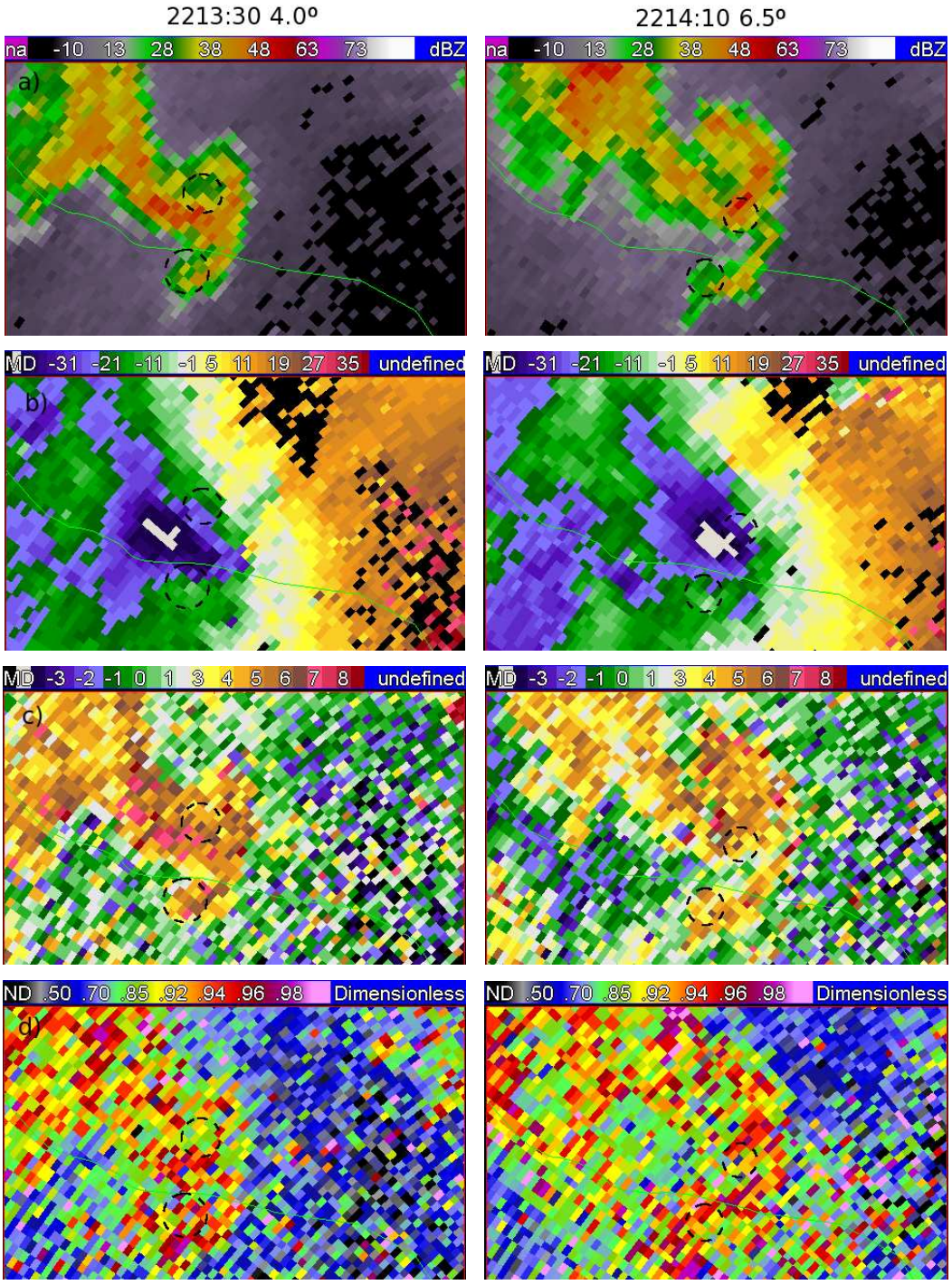

Figure 4: Spearhead echo observed at the 4.0° and 6.5° tilts in a) reflectivity, b) radial velocity, c) differential reflectivity Z_{DR}, and d) cross-correlation coefficient ρ_{hv} during the 2212 UTC volume scan.

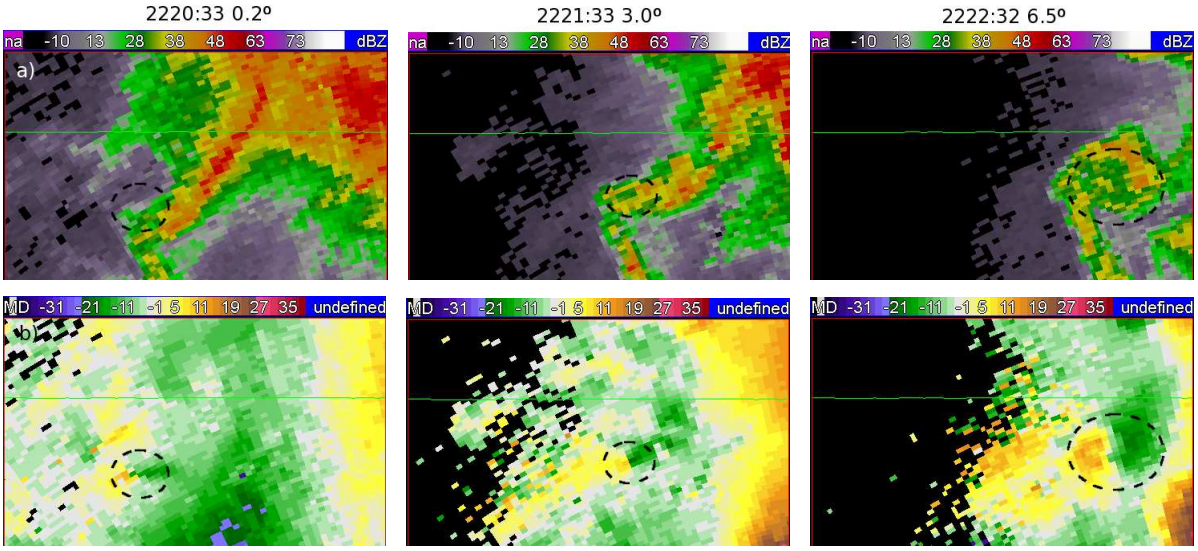

Figure 5: Mesoanticyclone observed during the 2220 UTC volume scan at 0.2°, 3.0°, and 6.5°, in a) reflectivity, and b) radial velocity. The anticyclonic azimuthal shear region is highlighted by the black circle, shown on both the reflectivity and radial velocity images. An embedded TVS is also observed at each tilt.

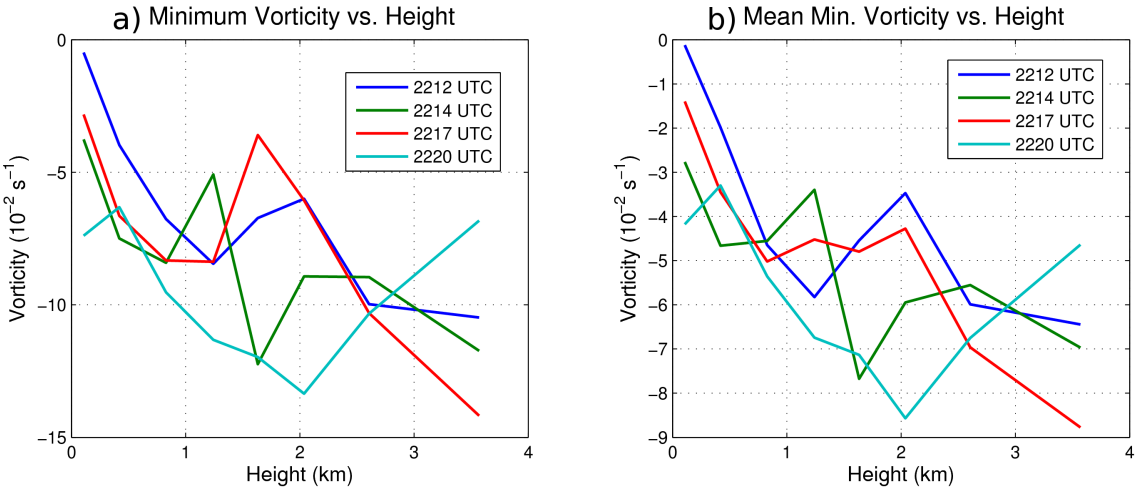

Figure 6: The a) minimum vorticity and b) mean minimum vorticity (computed over a 3-by-3 region) as a function of height between 2212 and 2220 UTC.

appear to have consolidated into larger vortices at 3.0° and 4.0° tilts (about 600 – 800 m AGL).

To investigate the structure and dynamics of the RFD gust front vortices, vorticity, divergence and the stretching term of the vorticity equation were computed, as described in Section 3. Figure 9 presents the mean vorticity, divergence and stretching term of the vorticity equation as a function of height, computed from nine different RFD gust front vortices at the center of the vortex. The mean vortex intensity (magnitude of the maximum and minimum vorticity) exceeded the minimum threshold for a mesocyclone of 10^{-2} s^{-1}, and the maximum vorticity was near or above the threshold for a weak tornado of 10^{-1} s^{-1}, even at the lowest elevation angle (about 90 m AGL). Hence, this suggests that gustnadoes may have been present along the RFD gust front as strong rotation was observed very close to the surface; however, the spatial resolution is probably too small to resolve the individual gustnadoes, which have diameters on the order of 100 – 200 m (e.g., Wilson, 1986).

The RFD vortices exhibited varying intensities, orientation, and diameter as a function of height. The vortex intensity increased as a function of height from the surface to 1 – 1.5 km AGL, and then decreased for cyclonic vortices and decreased slightly for anticyclonic vortices. A discussion of the vorticity variations in height will follow in the next section, invoking the vertical vorticity equation for analysis. Figure 10 presents the mean vortex orientation relative to the motion of the RFD gust front, revealing that the vortices advect behind the RFD gust front. The transient nature of the vortices may be explained by the rearward advection of the vortices, away from the sources of positive vorticity generation (e.g., tilting of horizontal vorticity into the vertical and subsequent stretching).

2) Vertical vorticity equation analysis

As the RFD gust front penetrates the inflow region of the storm, convergence along it increases significantly. The increase in convergence along the RFD gust front also coincides with the development of these intense vortices along the RFD gust front. The computed divergence fields reveal strong convergence extending throughout the depth of the gust front vortices (Figure 9c), and divergence values of nearly -4 X 10^{-2} s^{-1} are observed at about 90 m AGL. Using the continuity equation to integrate the divergence as a function of height, the vertical velocities obtained within the RFD gust front vortices are about 40 m s^{-1}. Assuming a parcel at rest, the time required for the parcel to reach the highest tilt through the updraft in the RFD gust front (about 2.3 km) is 129 s.

Based on the vorticity and divergence as a function of height, the vorticity equation can be used to understand how intense vortices develop along the RFD gust front. Unfortunately, without a dual-Doppler analysis, only the stretching term (Equation 4) can be assessed under the assumption that the unobserved component of divergence is relatively small. The stretching term of the vorticity equation is also computed for each height (Figure 9d), and reveals that the stretching term generally decreases as a function of height. The order magnitude of the stretching term is about 10^{-3} s^{-2}, and reaches a maximum of 10^{-3} s^{-2} at about 90 m AGL. Hence, a relatively weak vortex possessing vorticity values of 10^{-3} s^{-1} could intensify into a gustnado or weak tornado (vorticity of 10^{-1} s^{-1}) in only 100 s, based on stretching term on the order of 10^{-3} s^{-2}.

4.4. Tornadogenesis and Tornado Intensification

The first tornadic debris signature (TDS; Ryzkhov et al., 2002; Ryzhkov et al., 2005; Bluestein et al., 2007; Kumjian and Ryzhkov, 2008) appeared at 2226 UTC, characterized by low ρ_{hv} (< 0.7) and a relative minimum in Z_{DR} (Figure 11). The negative values of Z_{DR} of -2 to -5 dB are the result of differential attenuation through the forward-flank downdraft (FFD) of the supercell storm to the south. In reflectivity to the west of the tornado, the hook echo appears disconnected from the tornado. A ring of precipitation surrounds the tornado, with small drop sizes indicated by high ρ_{hv} ($>$ 0.96) and a relative minimum in Z_{DR} values, and low drop concentration indicated by low reflectivity.

A dramatic intensification in the Moore tornado occurs between 2226 and 2231 UTC. Table 1 shows the evolution of the maximum radial velocity, velocity difference, diameter, and maximum vorticity during this period. The diameter of the tornado is defined as the distance between minimum and maximum radial velocities in the tornado. At 2226 UTC, the maximum radial velocities and velocity difference are 38.1 and 50.9 m s^{-1}, respectively, and the diameter was 560 m. The tornado intensified slightly between 2228 UTC, exhibiting a slightly larger diameter and maximum radial velocities and velocity differences of 51.4 and 79.2 m s^{-1}, respectively. Over the next volume scan, the diameter of the tornado increased by nearly a factor of 3! The tornadic debris signature also increases significantly in width, with a large region of very low ρ_{hv} and high Z_{DR} values observed within the tornado. The maximum radial velocities observed of 73.5 m s^{-1} are just below the threshold for EF-4 tornado winds.

During the period of intensification, the tornado moves closer to the mid-level mesocyclone. At 2226 and 2228 UTC, the displacement between the tornado and the mid-level mesocyclone at 9.0° is 3.3 and 3.1 km, respectively (Table 1). Between the 2228 and 2231 UTC scans, the tornado moves under the mid-level mesocyclone, and is located just 0.9 km from the center of the mid-level mesocyclone at 2231 UTC. One explanation for the rapid

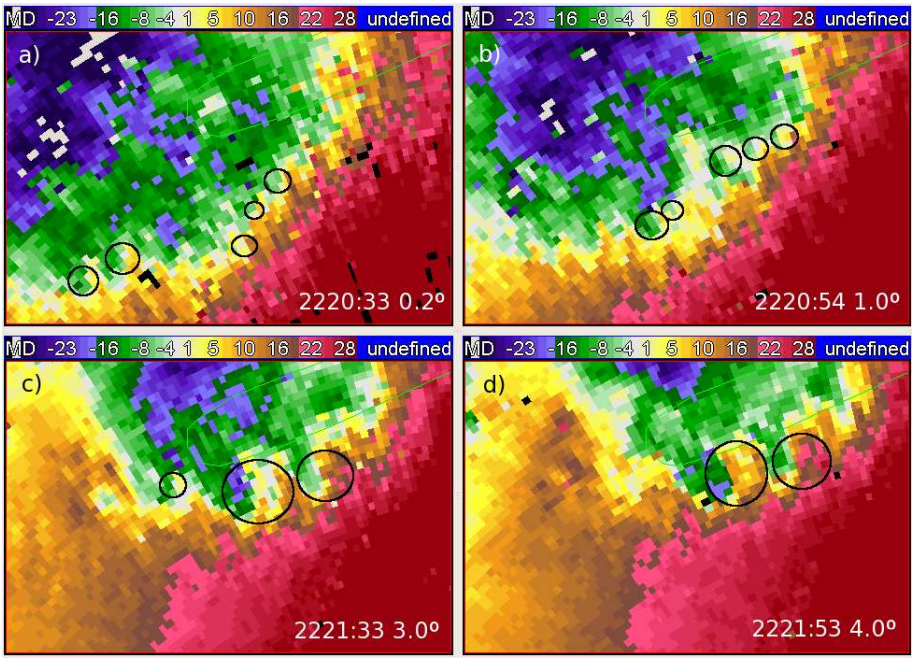

Figure 8: Radial velocity between 2220:33 and 2221:53 UTC at a) 0.2°, b) 1.0°, c) 3.0°, and 4.0° tilts, zoomed in on the RFD gust front. Individual azimuthal shear zones, indicative of vortices, are indicated by the black circles. The scale of the vortices increases and the concentration decreases as a function of height.

intensification of the tornado during this period is an increase in the stretching of low-level vertical vorticity by the updraft as the tornado moves beneath the center of the mid-level mesocyclone.

The ring of precipitation surrounding the tornado evolves significantly between 2226 and 2231 UTC. By 2231 UTC, a ring of moderate Z_{DR} (2 – 4 dB) and moderate ρ_{hv} values surround the tornado, indicating an increase in drop sizes in the precipitation surrounding the tornado. A broad region of large drops flanks the left side of the tornado, but drops are concentrated in two smaller bands of higher reflectivity. To the east of the tornado, a band of small drops is drawn northward from the FFD of the supercell to the south. The small drop sizes are implied by very high ρ_{hv} values (> 0.97) and low Z_{DR} values (0 – 2 dB). The reflectivity in the small drop region is between 30 – 40 dBZ, implying a relatively high concentration of small drops.

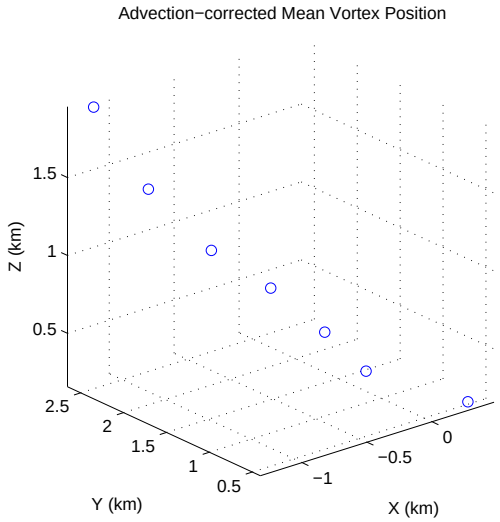

Figure 10: Mean position of the RFD gust front vortices in Cartesian coordinates, where (x=0 km, y=0 km, z=0 km) is the position of the RFD gust front vortex at the lowest elevation angle.

5. DISCUSSION

This study examines several intense, small-scale vortices within a supercell, located along the periphery of the hook echo and along the trailing RFD gust front. This section discusses the origins of these small-scale vortices and their possible role in mesocyclone evolution and tornadogenesis.

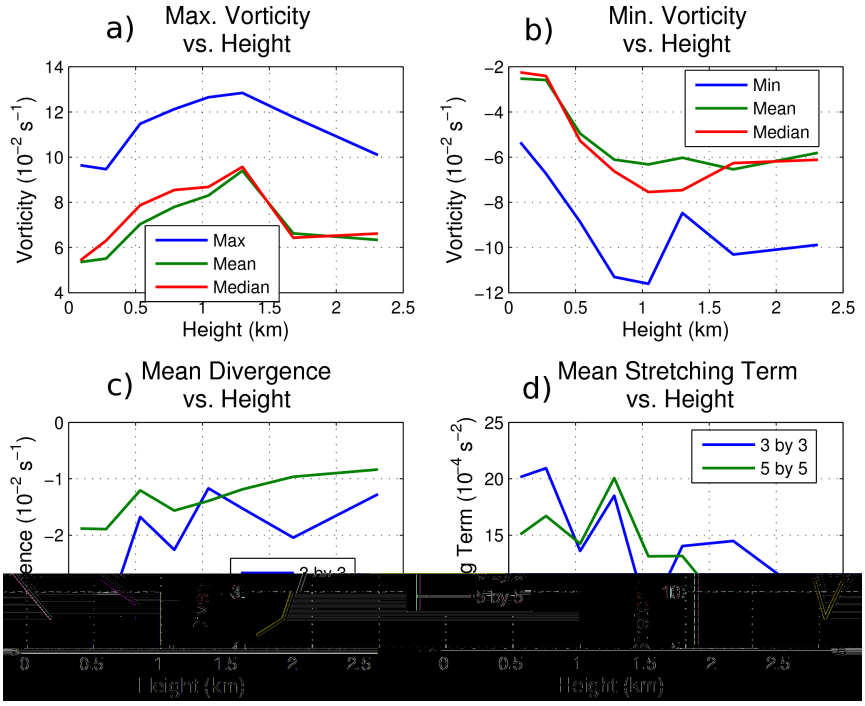

Figure 9: a) Maximum, mean, and median vorticity (mean and median calculated over 3-by-3 region) in cyclonic shear regions, b) minimum, mean, and median vorticity in anticyclonic shear regions, c) mean divergence, and d) mean stretching term. These quantities are computed as a function of elevation angle to analyze how the vortices change dynamically with height.

Table 1: Maximum radial velocity, velocity difference, diameter, maximum vorticity of the tornado, and the displacement between the tornado and mid-level mesocyclone (MC displacement), during the intensification between 2226 and 2231 UTC 10 May 2010.

Time (UTC)	Max. v_r (m s^{-1})	Velocity Difference (m s^{-1})	Diameter (km)	Max. Vorticity (s^{-1})	MC Displacement (km)
2226:32	38.1	50.9	0.56	0.22	3.3
2228:53	51.4	79.2	0.63	0.34	3.1
2231:14	73.5	109.0	1.95	0.28	0.9

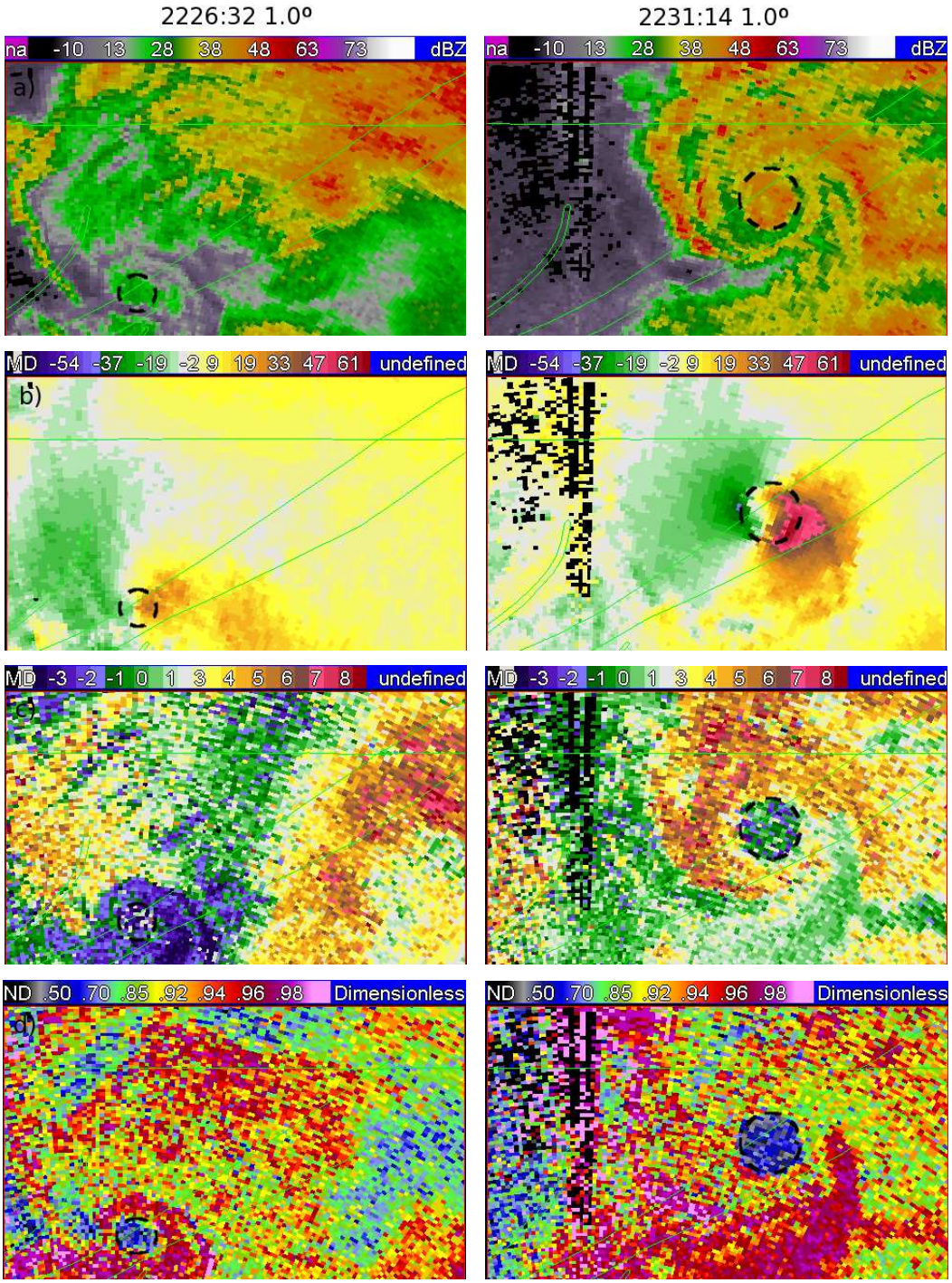

Figure 11: Tornado evolution between 2226 and 2231 UTC at the 1.0° tilt, in a) reflectivity, b) radial velocity, c) differential reflectivity Z_{DR}, and d) cross-correlation coefficient ρ_{hv}.

A possible origin of the vortices along the periphery of the hook echo is from outflow from nearby dissipating convection. During the 2206 UTC volume scan, a region of outflow is indicated by very high ρ_{hv} values (Figure 2d), indicative of small drops from dissipated convection. This high ρ_{hv} region can be tracked from dissipating convection to the south during previous volume scans (not shown). These vortices could result from tilting of horizontal vorticity, generated along the leading edge of the outflow, into the vertical by the RFD. A counterrotating vortex pair would result on each side of the hook echo, which is observed in Figure 2. Another candidate for the origins of these vortices is tilting of low-level, environmental horizontal vorticity (e.g., horizontal convective rolls or HCRs). However, the relatively uniform distance between HCRs would likely produce regularly spaced vortices along the hook echo, resulting from the tilting of HCRs along the hook echo at regular intervals. In the present case, only one pair of counter-rotating vortices is observed along the hook echo.

Vortices with a relatively uniform spacing of approximately 1.5 km (twice the diameter) are generated along the RFD gust front during the 2200 and 2223 UTC volume scans. Since HCRs are generally uniformly spaced horizontally, the uniform spacing of vortices along the RFD gust front could result from tilting of HCRs into the vertical. This is consistent with previous studies, which also identified tilting of low-level environmental vorticity as a source of vorticity along the RFD gust front (e.g., Dowell and Bluestein, 2002a,b).

Vortices along the periphery of the hook echo probably did not play a role in tornadogenesis. These vortices were relatively transient, and the vortices did not interact with the developing mesocyclone. These vortices exist during the early stages of the hook echo and RFD, and prior to the development of intense low-level rotation. However, such vortices produced by outflow interactions might play a role in tornadogenesis if they interact with the low-level mesocyclone during tornadogenesis. In contrast to the vortices along the periphery of the hook echo, the RFD gust front vortices form during the RFD gust front surge which occurs during the intensification of the low-level mesocyclone and, subsequently, tornadogenesis. The RFD gust front vortices form beginning around 2217 UTC, and persist even after the tornado intensified significantly. Owing to the regular pattern of vortices along the RFD gust front and the 2.5 min between volume scans, it was not possible to distinguish individual vortices along the RFD gust front except for vertical continuity (about 20 s between tilts). A more thorough examination of possible vortex mergers during tornadogenesis is planned. However, the limited temporal resolution could inhibit observations of vortex mergers and the ensuing rapid changes in mesocyclone intensity.

6. SUMMARY AND CONCLUSIONS

The first part of this paper investigates small-scale vortices forming along the periphery of the hook echo and along the RFD gust front. The vortices along the outside periphery of the hook echo were anticyclonic, whereas the vortices along the inside periphery of the hook echo were cyclonic. Small-scale vortices along the periphery of the hook echo reach mesocyclone intensity, produce reflectivity flares extending outward from the hook echo, and contribute to the contorted structure of the hook echo. In most cases, the drop sizes and hydrometeor types deduced from polarimetric data revealed similar precipitation in the hook echo and these reflectivity flares, indicating that horizontal advection by the vortices produced the reflectivity flares. However, in one case, the weaker anticyclonic vortex exhibited more curvature, whereas the stronger cyclonic vortex is nearly precipitation-free.

A persistent mesoanticyclone was observed over several volume scans, with vorticity values reaching weak tornado intensity. The diameter of the mesoanticyclone increased as a function of height, and a full ring of precipitation surrounded the mesoanticyclone at the 6.5° tilt. The vorticity magnitude within the mesoanticyclone generally increased as a function of height, and increased as a function of time at the lowest tilt. A remarkable feature of the mesoanticyclone was the extreme tilt in the horizontal, as the mesoanticyclone was more tilted in the horizontal than the vertical!

Intense vortices developed along the RFD gust front, and nine coherent vortices were examined to understand the characteristics of these vortices. As a function of height, the mean vortex diameter of these gust front vortices increased and the concentration of vortices decreased. The smaller scale vortices within the lowest 100 – 200 m consolidate into larger scale vortices at about 700–800 m AGL. The maximum vorticity values associated with these RFD gust front vortices approached or exceeded the threshold for weak tornadoes, indicating that weak gustnadoes may have occurred along the RFD gust front. The vortex intensity increased as a function of height in the lowest 1 – 1.5 km, and then decreased as a function of height above 1.5 km. A limited, yet revealing analysis of the vorticity equation showed that the stretching term was on the order of 10^{-3} s^{-2}. Thus, intense near-surface convergence along the RFD gust front likely played a significant role in producing these intense vorticity maxima along the RFD gust front. Vertical velocities along the gust front in the vicinity of the vortices reached nearly 40 m s^{-1} at about 2.5 km AGL.

The tornado intensified quickly after tornadogenesis, increasing in diameter by a factor of three in just 2.5 min. Polarimetric data reveal that the environment surrounding the tornado is quite inhomogeneous, and evolves very quickly. Initially, the tornado was surrounded by a ring

of precipitation characterized by small drop sizes. After intensification, a full ring of precipitation characterized by large drop sizes surrounds the tornado, and a band of small drops wraps around from the supercell to the south. The origins of the precipitation might indicate characteristics of the air ingested by the tornado. For example, large drop sizes may result from size sorting within the mesocyclone (Kumjian and Ryzhkov, 2009), so the presence of large drops could imply higher angular momentum air from the mesocyclone reaching the surface. Markowski et al. (2003) and Davies-Jones (2008) discuss the role of the RFD in transporting higher angular momentum air to the surface, where the air converges under the updraft and a tornado forms. These observations could result from corner flow collapse (Lewellen, 2007; Lewellen and Lewellen, 2007), in which low angular momentum inflow air is impeded and higher angular momentum replaces it from aloft. In this case, higher angular momentum air from aloft might contribute to the intensification of the tornado.

A novel aspect of this study is an investigation of low-level hook echo structure, including the role of advection using polarimetric data and an analysis of a strong mesoanticyclone. The relative contributions of horizontal advection and the descent of precipitation around the RFD remain an open question. Using polarimetric data, most vortices within the RFD advected precipitation outward, producing reflectivity flares along the hook echo. However, in some cases, horizontal advection did not fully explain hook echo structure. Relatively little attention is given to the mesoanticyclone in the literature, primarily because mesoanticyclones produce tornadoes much less frequently than mesocyclones. However, intense anticyclonic shear was observed at 100 m AGL, perhaps indicative of a brief anticyclonic tornado. Moreover, a prominent weak echo region is also observed at the center of the mesoanticyclone.

While previous studies have observed small-scale vortices along the RFD gust front (Bluestein et al., 1997, 2003), this paper examines characteristics of several RFD gust front vortices, including the intensity, diameter, and orientation of the vortices. The very dense vertical sampling and proximity to the radar provided very good vertical resolution of these vortex characteristics, and previous studies did not have sufficient clear-air observations to utilize velocity data quantitatively. The convergence, vertical velocity, and stretching terms along the RFD gust front were computed, revealing that the RFD gust front vortices were intensified at low-levels by intense vortex stretching.

Since only a limited analysis of the vorticity equation was possible from single-Doppler observations, dual-Doppler analyses are needed to fully evaluate the terms of the vorticity equation. In particular, dual-Doppler analyses may reveal what the origins of the vortices (e.g., tilting), or what causes the dissipation of the vortices (e.g., moving into a region of divergence). Moreover, dual-Doppler analyses could investigate the origins of the complex precipitation structure observed around the tornado if trajectory analyses can be performed. Dual-Doppler analyses are planned with OU-PRIME and other Norman-based radars, including the National Weather Radar Testbed Phased Array Radar (e.g., Zrnić et al., 2007) or the Oklahoma City, Oklahoma (KTLX) Weather Surveillance Radar-1988 Doppler (WSR-88D).

7. ACKNOWLEDGMENTS

OU-PRIME is maintained and operated by the Atmospheric Radar Research Center (ARRC) of the University of Oklahoma. This paper also benefited from discussions with Chris Schwarz, Matt Kumjian, and Brad Isom. Doug Speheger provided tornado damage paths produced by the Norman, OK NWS WFO, and provided further details about the tornado damage. The authors also thank Boon Leng Cheong, Redmond Kelley, Adam Smith and Pengfei Zhang for their assistance with computing issues, and thank Boon Leng Cheong for operating the radar during the 10 May 2010 outbreak. The first author was also partially supported by an University of Oklahoma Alumni Fellowship.

References

Bluestein, H. B., M. M. French, R. L. Tanamachi, S. Frasier, K. Hardwick, F. Junyent, and A. Pazmany, 2007: Close-range observations of tornadoes in supercells made with a dual-polarization, X-band, mobile Doppler radar. *Mon. Wea. Rev.*, **135**, 1522–1543.

Bluestein, H. B., S. G. Gaddy, D. C. Dowell, A. L. Pazmany, J. C. Galloway, R. E. McIntosh, and H. Stein, 1997: Doppler radar observations of substorm-scale vortices in a supercell. *Mon. Wea. Rev.*, **125**, 1046–1059.

Bluestein, H. B., C. C. Weiss, and A. L. Pazmany, 2003: Mobile Doppler radar observations of a tornado in a supercell near Bassett, Nebraska, on 5 June 1999. Part I: Tornadogenesis. *Mon. Wea. Rev.*, **131**, 2954–2967.

Bodine, D., R. D. Palmer, M. R. Kumjian, and A. V. Ryzhkov, 2010: High-resolution OU-PRIME radar observations of a prolific tornado-producing supercell on 10 May 2010. in A. M. Soc., editor, *25th Conf. on Severe Local Storms*, Denver, CO.

Browning, K. A., 1964: Airflow and precipitation trajectories within severe local storms which travel to the right of the winds. *J. Atmos. Sci.*, **21**, 634–639.

Burgess, D. W., V. T. Wood, and R. A. Brown, 1982: Mesocyclone evolution statistics. in A. M. Soc., editor, *Preprints, 12th Conf. on Severe Local Storms*, pp. 422–424, San Antonio, TX.

Charba, J., and V. Sasaki, 1971: Sturcture and movement from severe thunderstorms of 3 April 1964 as revealed by radar and surface mesonetwork data analysis. *J. Meteor. Soc. Japan*, **49**, 191–213.

Davies-Jones, R., 2008: Can a descending rain curtain in a supercell instigate tornadogenesis barotropically? *J. Atmos. Sci.*, **65**, 2469–2497.

Dowell, D. C., and H. B. Bluestein, 2002a: The 8 June 2005 McLean, Texas storm. Part I: Observations of cyclic tornadogenesis. *Mon. Wea. Rev.*, **130**, 2626–2648.

Dowell, D. C., and H. B. Bluestein, 2002b: The 8 June 2005 McLean, Texas storm. Part II: Cyclic tornado formation, maintenance, and dissipation. *Mon. Wea. Rev.*, **130**, 2649–2670.

Forbes, G. S., 1981: On the reliability of hook echoes as tornado indicators. *Mon. Wea. Rev.*, **109**, 1457–1466.

French, M. M., H. B. Bluestein, D. C. Dowell, L. J. Wicker, M. R. Kramar, and A. L. Pazmany, 2008: High-resolution, mobile Doppler radar observations of cyclic mesocyclogenesis in a supercell. *Mon. Wea. Rev.*, **136**, 4997–5016.

Fujita, T. T., 1958: Mesoanalysis of Illinois tornadoes of 9 April 1953. *J. Meteor.*, **15**, 288–296.

Fujita, T. T., and H. R. Byers, 1977: Spearhead echo and downburst in the crash of an airliner. *Mon. Wea. Rev.*, **105**, 129–146.

Kumjian, M. R., and A. V. Ryzhkov, 2008: Polarimetric signatures in supercell thunderstorms. *J. Appl. Meteor. Climatol.*, **48**, 1940–1961.

Kumjian, M. R., and A. V. Ryzhkov, 2009: Storm-relative helicity revealed from polarimetric radar measurements. *J. Atmos. Sci.*, **66**, 667–685.

Lei, L., G. Zhang, R. D. Palmer, B. L. Cheong, and M. Xue, 2009: A multi-lag correlation estimator for polarimetric radar variables in the presence of noise. in *34th Conf. on Radar Meteorology*, Williamsburg, VA. Amer. Meteor. Soc.

Lewellen, D. C., 2007: Near-surface intensification of tornado vortices. *J. Atmos. Sci.*, **64**, 2176–2194.

Lewellen, D. C., and W. S. Lewellen, 2007: Near-surface vortex intensification through corner flow collapse. *J. Atmos. Sci.*, **64**, 2195–2209.

Magsig, M. A., D. W. Burgess, D. C. Dowell, Y. P. Richardson, and J. M. Wurman, 2002: The structure and evolution of hook echoes during tornadogenesis as revealed by high resolution radar data. in A. M. Soc., editor, *21st Conf. on Severe Local Storms*, San Antonio, TX.

Magsig, M. A., and D. C. Dowell, 2004: Evolution of the hook echo and low-level rotation in the 17 May 2000 Brady, NE supercell. in A. M. Soc., editor, *22nd Conf. on Severe Local Storms*, Hyannis, MA.

Markowski, P. M., 2002: Hook echoes and rear-flank downdrafts: A review. *Mon. Wea. Rev.*, **130**, 852–876.

Markowski, P. M., J. M. Straka, and E. N. Rasmussen, 2003: Tornadogenesis resulting from the transport of circulation by a downdraft: Idealized numerical simulations. *J. Atmos. Sci.*, **60**, 795–823.

Oye, R. C., K. Mueller, and S. Smith, 1995: Software for radar translation, editing, and interpolation. in *Preprints, 27th Conf. on Radar Meteorology*, pp. 359–361, Vail, CO. Amer. Meteor. Soc.

Palmer, R. D., D. Bodine, M. Kumjian, B. Cheong, G. Zhang, Q. Cao, H. B. Bluestein, A. Ryzkhov, T.-Y. Yu, and Y. Wang, 2010: The 10 May 2010 tornado oiutbreak in central Oklahoma: Potential for new science with high-resolution polarimetric radar. *Bull. Amer. Meteor. Sci.*, **submitted**.

Palmer, R. D., A. V. Ryzhkov, G. Zhang, B. L. Cheong, T.-Y. Yu, M. B. Yeary, P. B. Chilson, M. I. Biggerstaff, N. L. Hickmon, R. J. Doviak, D. S. Zrnić, M. Knight, N. E. Lawrence, F. Sloan, C. Goode, R. Stafford, R. Keene, P. Neilley, A. Turnbill, J. T. Snow, T. H. L. Williams, and D. Marsh, 2009: OU-PRIME: a high-resolution platform for interdisciplinary polarimetric radar research and education at the University of Oklahoma. in *34th Conf. on Radar Meteorology*, Williamsburg, VA. Amer. Meteor. Soc.

Ryzhkov, A. V., T. J. Schuur, D. W. Burgess, and D. S. Zrnić, 2005: Polarimetric tornado detection. *J. Appl. Meteor.*, **44**, 557–570.

Ryzkhov, A., D. Burgess, D. Zrnić, T. Smith, and S. Giangrande, 2002: Polarimetric analysis of a 3 May 1999 tornado. in A. M. Soc., editor, *Preprints, 22th Conf. on Severe Local Storms*, Hyannis, MA.

Sirmans, D., D. Zrnić, and B. Bumgarner, 1976: Extension of maximum unambiguous Doppler velocity by use of two sampling rates. in A. M. Soc., editor, *Proc. 17th Conf. on Radar Meteorology*, pp. 23–28.

Smith, T. M., and K. L. Elmore, 2004: The use of radial velocity derivatives to diagnose rotation and divergence. in *11th Conf. on Aviation, Range and Aerospace*, Hyannis, MA. Amer. Meteor. Soc.

Trapp, R. J., G. J. Stumpf, and K. L. Manross, 2005: A reassessment of the percentage of tornadic mesocyclones. *Wea. Forecasting*, **20**, 680–687.

Wakimoto, R. M., H. V. Murphey, A. Nester, D. P. Jorgensen, and N. T. Atkins, 2006: High winds generated by bow

echoes. part I: Overview of the Omaha bow echo 5 July 2003 storm during BAMEX. *Mon. Wea. Rev.*, **134**, 2793–2812.

Wicker, L. J., and R. B. Wilhelmson, 1995: Simulation and analysis of tornado development and decay within a three-dimensional thunderstorm. *J. Atmos. Sci.*, **52**, 2675–2703.

Wilhelmson, R. B., and J. B. Klemp, 1981: A three dimensional numerical simulation of splitting severe storms on 3 April 1964. *J. Atmos. Sci.*, **38**, 1581–1600.

Wilson, J. W., 1986: Tornadogenesis by nonprecipitation induced wind shear lines. *Mon. Wea. Rev.*, **114**, 270–284.

Wurman, J., Y. Richardson, C. Alexander, S. Weygandt, and P.-F. Zhang, 2007: Dual-doppler and single-doppler analysis of a tornadic storm undergoing mergers and repeated tornadogenesis. *Mon. Wea. Rev.*, **135**, 736–758.

Zhang, G., R. Doviak, J. Vivekanandan, W. Brown, and S. A. Cohn, 2004: Performance of correlation estimators for spaced antenna wind measurement in the presence of noise. *Radio Sci.*, **39**, 3017–3033.

Ziegler, C. L., E. N. Rasmussen, T. R. Shepherd, A. I. Watson, and J. M. Straka, 2001: The evolution of low-level rotation in the 29 May 1994 Newcastle–Graham, Texas, storm complex during VORTEX. *Mon. Wea. Rev.*, **129**, 1339–1368.

Zrnić, D. S., J. F. Kimpel, D. E. Forsyth, A. Shapiro, G. Crain, R. Ferek, J. Heimmer, W. Benner, T. J. McNellis, and R. J. Vogt, 2007: Agile-beam phased array radar for weather observations. *Bull. Amer. Meteor. Sci.*, **88**, 1753–1766.